Xe-ion-irradiation-induced structural transitions and elemental diffusion in high-entropy alloy and nitride thin-film multilayers

Ji Wang [a],*, Rui Shu [b],*, Jianlong Chai [c], Smita G. Rao [b], Arnaud le Febvrier [b], Haichen Wu [d], Yabin Zhu [c], Cunfeng Yao [c], Laihui Luo [a], Weiping Li [a], Peifeng Gao [e],*, Per Eklund [b],*

[a] School of Physical Science and Technology, Ningbo University, Ningbo 315211, China
[b] Thin Film Physics Division, Department of Physics, Chemistry, and Biology (IFM), Linköping University, Linköping 58183, Sweden
[c] Institute of Modern Physics, Chinese Academy of Sciences, Lanzhou 730000, China
[d] Ningbo Institute of Materials Technology and Engineering, Chinese Academy of Sciences, Ningbo 315201, China
[e] Key Laboratory of Mechanics on Western Disaster and Environment, Ministry of Education, College of Civil Engineering and Mechanics, Lanzhou University, Lanzhou 730000, China

HIGHLIGHTS

- TiNbZrTa/CrFeCoNi metallic and nitride multilayers deposited by magnetron sputtering.
- Microstructural evolution of irradiated films using 3-MeV Xe^{20+} ion at different temperatures were studied.
- TiNbZrTa/CrFeCoNi nitride multilayers were retained with no observable atomic mixing among adjacent sublayer.
- TiNbZrTa/CrFeCoNi metallic multilayers exhibited interdiffusion and mixing under ion irradiation and/or heat treatment.

GRAPHICAL ABSTRACT
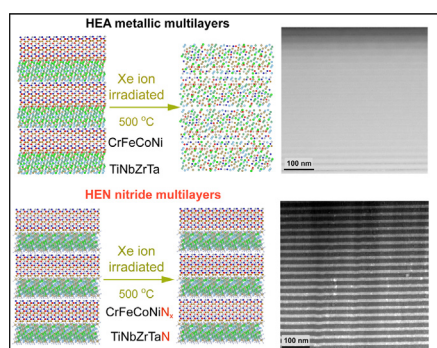
ARTICLE INFO

ABSTRACT

The study aims to understand the irradiation behavior of multilayer coatings composed of high-entropy materials. Here, we report the structural stability and elemental segregation of high-entropy TiNbZrTa/CrFeCoNi metallic and nitride multilayer coatings under 3-MeV Xe^{20+} ion-irradiation at room temperature and 500 °C, respectively. Transmission electron microscopy analysis shows that the microstructure of nanocrystalline CrFeCoNi high-entropy-alloy sublayers are not stable and readily transforms into amorphous state at 500 °C and/or under irradiation conditions. The elemental distribution, acquired by energy-dispersive X-ray spectroscopy under scanning transmission electron microscopy mode, shows preferential diffusion of Co and Ni into TiNbZrTa sublayers, while Fe and Cr preferentially remain within the previous CrFeCoNi sublayers. TiNbZrTaN/$CrFeCoNiN_x$ nitride multilayers exhibit a higher crystallinity and structural stability as well as resistance to diffusion at high-temperature and/or irradiation conditions than their TiNbZrTa/CrFeCoNi metallic multilayer counterparts. These findings are explained by atomic size differences, the difference in Gibbs free energy of the mixing system, and interstitial-solute-induced chemical heterogeneity. Our findings thus provide a design strategy of high entropy nitride for nuclear fuel cladding.

* Corresponding authors.
E-mail addresses: wangji1@nbu.edu.cn (J. Wang), rui.shu@liu.se (R. Shu), gaopf@lzu.edu.cn (P. Gao), per.eklund@liu.se (P. Eklund).

1. Introduction

Coating technology for nuclear fuel cladding is an innovative solution to increase the safety of advanced nuclear fission facilities [1,2]. Due to the harsh working environment, the coating materials in nuclear facilities are subject to a combination of high temperature, high pressure and intense irradiation fields [3]. Among the many factors that must be taken into consideration for candidate coating materials, intense irradiation is of crucial importance. A significant density of interstitials, vacancies, and the subsequent defect clusters in the serving materials are produced by the intense irradiation fluxes, which finally leads to a degradation of their thermomechanical properties [3]. Improving the irradiation resistance of these materials is a challenge driving studies towards the design of irradiation tolerant coatings. A strategy is adopting irradiation-resistant bulk materials into coatings, such as, employing irradiation-resistant high entropy alloys [4] and high entropy ceramics [5–8]. Another approach is introducing complex structures, for instance, multilayered structures to increase density of interfaces for the annihilation of irradiation induced defects [9]. This method has been used for a range of multilayer nanostructured systems, including crystalline/amorphous multilayers (W/Si [10], Cu/Ta[11]) and crystalline/crystalline multilayers, such as, face-centered cubic phase (*fcc*)/body-centered cubic (*bcc*) (Cu/Nb [9], Cu/V[12]), *fcc*/*fcc* (Cu/Ag[13], Ag/Ni[14], CrN/ZrN[15]), *bcc*/*bcc* (Fe/W[16]), hexagonal close-packed phase (*hcp*)/*fcc* (AlN/TiN[17]).

High-entropy alloys (HEAs) [18,19] were originally defined as a mixture of five or more elements with concentrations between 5 and 35 atomic percent, forming a solid-solution phase as *bcc*, *fcc*, or *hcp* through suppressing the formation of intermetallic compounds. Generally, two main groups of notable HEAs can be classified for use at high temperatures: (i) *fcc* HEAs based on the 3d-transition metals Cr, Mn, Co, Fe, Cu and Ni, which also referred to as the Cantor alloy [19]; (ii) *bcc* HEAs [20] based on refractory elements, Ti, Zr, Hf, V, Nb, Ta, Mo and W. Compared to conventional alloys containing one or two base elements, HEAs possess good mechanical properties, corrosion resistance, and irradiation resistance [21,22]. Addition of a small amount of C and N in the HEAs can improve the irradiation resistance of the parent-HEAs by increasing lattice distortion and roughening atomic-level energy landscape [6,23]. High entropy nitrides (HENs) [24], a class of ceramic materials based on HEA concept, but with dissolved nitrogen, have been studied as protective coatings for cutting tools [25,26], diffusion barrier layers [27], and corrosion resistant coatings [28] are now finding application as irradiation resistant coatings [7,29]. Combining the good irradiation resistance of HEAs and HENs with merits such as mechanical and defect-annihilating-promotion properties of multilayered structures, the irradiation resistant behavior of the novel HEA/HEA and HEN/HEN multilayer films and the underlying mechanism are worthy of investigation. In particular, there is a need to study the microstructural stability and elemental diffusion at high temperature and irradiation conditions.

In the present work, high-entropy TiNbZrTa/CrFeCoNi metallic and nitride multilayer films, with multilayer periods about 30 nm and a total thickness of ∼ 2 μm, were grown on *c*-sapphire substrates using magnetron sputtering. Subsequent Xe-ion-irradiation experiments were carried out on the multilayer systems at room temperature and 500 °C to introduce a high irradiation damage. Microstructural analysis based on transmission electron microscopy (TEM), selected area electron diffraction (SAED) and energy dispersive X-ray spectroscopy in scanning transmission electron microscopy mode (STEM-EDX) were conducted on the multilayers irradiated at RT and 500 °C to investigate the irradiation response, including structural stability, atomic mixing, and the underlying mechanisms.

2. Experimental details

The high-entropy alloy and nitride multilayers were deposited on $Al_2O_3(0001)$ by (reactive) magnetron sputtering in an ultrahigh vacuum chamber (base pressure < 10^{-8} Pa). A detailed description of the deposition system can be found elsewhere [30]. For metallic multilayer films, the alternate deposition was carried out with constant direct-current power of 100 W for two compound targets of $Ti_{25}Nb_{25}Zr_{25}Ta_{25}$ and $Cr_{24}Fe_{32}Co_{24}Ni_{20}$. The Ar gas flow rate was kept at 80 sccm corresponding to a total pressure of 0.5 Pa (4 mTorr). For nitride multilayer films, the target power was both set at 200 W for two compound targets of $Ti_{25}Nb_{25}Zr_{25}Ta_{25}$ and $Cr_{35}Fe_{29}Co_{21}Ni_{15}$. The Ar/N_2 gas (75% Ar and 25 % N_2) flow rate was kept at 80 sccm corresponding to a total pressure of 0.5 Pa (4 mTorr). A pause time of 5 s was applied between each sublayer during alternate deposition. All the targets were manufactured by Plansee Composite Materials GmbH. $Al_2O_3(0001)$ substrates with a size of 10 × 10 mm^2 were cleaned sequentially with acetone and ethanol in an ultrasonic bath for 10 min, and finally blow-dried with nitrogen gas. The substrate holder was rotating and maintained electrically floating along with non-intentional heating ("room temperature", RT). The bilayer thickness was tuned to 30 nm by varying the sputter time of the individual targets, and the total deposition time was controlled to yield a thickness of 2 μm for both metallic and nitride multilayer films.

The elemental compositions of the individual TiNbZrTa and CrFeCoNi nitride films were determined using energy-dispersive X-ray spectrometry (EDX, Oxford Instruments X-Max) and time-of-flight elastic recoil detection analysis (ToF-ERDA) measurements. ToF-ERDA measurements were performed using a 40 MeV $^{127}I^{9+}$ beam at 67.5° incidence relative to the surface normal and a 45° recoil angle [31]. The data were analyzed using the simulation code Potku [32]. The content of the light elements nitrogen and oxygen were determined from ToF-ERDA, while the content of metals was determined by a combination of EDX and ToF-ERDA, due to the overlap between Zr and Nb and between Hf and Ta in ToF-ERDA coincidence mappings. The relative accuracy in obtaining the concentration of light elements by ToF-ERDA is better than 1.0 at.% given sufficient statistics, with high absolute accuracy demonstrated for nitrides[33].

X-ray diffraction (XRD) was carried out on a PANalytical X'Pert powder diffractometer with a Cu source ($\lambda_{K\alpha}$ = 1.5406 Å) operated at 45 kV/40 mA. Cross-sectional specimens for TEM were prepared by Focused Ion Beam (FIB, Thermo Fisher, Helios G4 CX) lift-out technique. Scanning transmission electron microscopy under high angle annular dark field (STEM-HAADF) mode and energy-dispersive X-ray spectroscopy (STEM-EDX) analysis, with a Super-X EDX detector, were performed in Talos F200X transmission electron microscope operated at 200 kV.

The irradiations were carried out using 3-MeV Xe ions along the surface normal direction to a fluence of 2 × 10^{15} ions/cm^2 at a terminal chamber of the 320 kV multi-discipline research platform for highly charged ions at the Institute of Modern Physics (IMP) in Lanzhou, China. The irradiation experiments were conducted at RT and 500 °C. The vacuum state in the terminal chamber during the irradiation procedure is ∼ 10^{-5} Pa. The Stopping and Range of Ions in Matter code (SRIM-2003 [34]) in Kinchin-Pease mode was used to estimate the displacement damage caused by 3 MeV Xe in a fluence of 2 × 10^{15} ions/cm^2, as shown in Fig. 1. The irradiation dose distribution shows the predicted damage profile extending from the surface to a depth of ∼ 1000 nm, with a peak damage of 13.3 dpa at ∼ 400 nm for the TiNbZrTa/CrFeCoNi metallic multilayers and a penetration depth of ∼ 1500 nm, with a peak damage of 7.6 dpa at ∼ 640 nm for the TiNbZrTa/CrFeCoNi nitride multilayers.
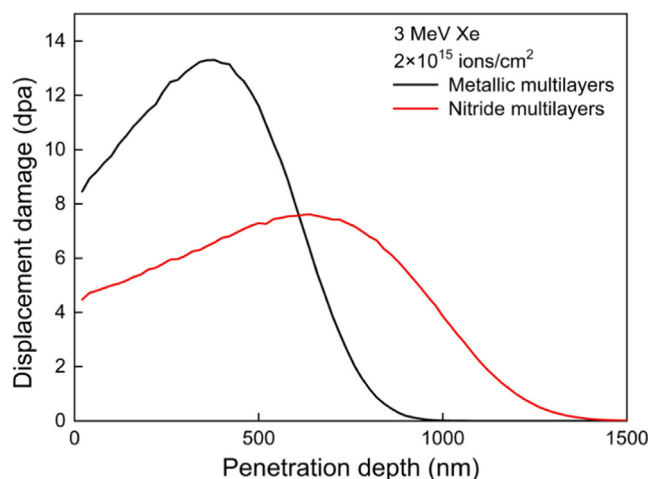
Fig. 1. Displacement damage as a function of depth for the TiNbZrTa/CrFeCoNi metallic and nitride multilayers irradiated with 3-MeV Xe ions.

3. Results

3.1. XRD

Fig. 2 shows θ-2θ X-ray diffractograms of the pristine metallic and nitride multilayers, and their corresponding multilayers irradiated at RT and 500 °C. Here, we will use the notations *fcc1*, *fcc2*, and *fcc3* to denote three different structures with face-centered cubic lattices: CrFeCoNi, TiNbZrTaN (NaCl-type), and CrFeCoNiN$_x$ (NaCl-type), respectively. For the metallic multilayers in Fig. 2a, the diffraction pattern shows a sharp peak near 43° assigned to *fcc1* (1 1 1) texture of CrFeCoNi and Pendellösung fringes located beside this peak. The formation of these fringes originating from interference between substrate, different sublayers and their interfaces, are commonly observed in superlattices and multilayered structures, such as TiN/SiN[35], W/Ni [36], and Cu/W [37]. On irradiating the pristine sample at room temperature, the intensity of *fcc1* (1 1 1) decreases and the interference fringes disappear. The same is also observed when irradiating at higher temperatures of 500 °C as shown in Fig. 2b. A broad feature appearing at 38° originates from an amorphous structure of the TiNbZrTa sublayers in metallic multilayers. In Fig. 2c and d, additional peaks are observed in nitride multilayers at 2θ values of ~ 34.7°, ~40.6° and 46.2, which correspond to the *fcc2* 111 and *fcc2* 200 of TiNbZrTaN sublayers and *fcc3* (2 0 0) texture CrFeCoNi nitrides of sublayers respectively. With increasing temperature, the *fcc2* (2 0 0) peak shifts to larger angle along with a decrease in the peak intensity when compared with the metallic multilayer (Fig. 2a). For the nitride multilayers irradiated at 500 °C, the 200-textured *fcc3* phase in CrFeCoNiN$_x$ sublayers is transformed into an *fcc1* phase (see Fig. 2d).

3.2. Microstructural characterization of multilayers irradiated at RT

Fig. 3 shows a comparison of microstructural evolution between metallic and nitride multilayers irradiated at RT. A significant contrast discrepancy in the metallic multilayers can be clearly observed at a depth of ~ 600 nm in Fig. 3a (a bright-field TEM image, BFTEM), which is caused by the ion irradiation. However, the experimentally observed irradiated depth of 600 nm does not match well with the predicted profiles calculated by SRIM code as shown in Fig. 1. This deviation may be because the target materials in SRIM simulation were assumed to be amorphous with homogeneously mixed elements while compositional elements are heterogeneously distributed in multilayer systems. Moreover,

the presence of interfaces between adjacent sublayers provides additional scattering sites for the incident ions [38]. SAED patterns of the metallic multilayers are presented in Fig. 3a, right top and bottom recorded from unirradiated region (circled region 1) and irradiated region (circled region 2), respectively. SAED pattern 1 acquired far from irradiation damage displays the microstructure of the as-deposited metallic multilayers. Two diffraction patterns can be observed, i.e., a ring like pattern originating from an amorphous phase and a set of diffraction spots which can be assigned to a 111-plane textured *fcc1* phase. Combined with the above analysis for the XRD pattern of as-deposited metallic multilayers and the information from HRTEM and FFT patterns from individual sublayers (Fig. 3b), it is easy to deduce that the amorphous phase originates from TiNbZrTa sublayers whereas CrFeCoNi sublayers contribute to the *fcc1* phase of as-deposited metallic multilayers. After irradiation by Xe-ions, the crystal structure of the CrFeCoNi layers were amorphized, which is confirmed by the amorphous bright ring in SAED pattern 2 and a significant amorphous feature presented in HRTEM in Fig. 3c.

The nitride multilayers irradiated at RT shows less contrast discrepancy in the BFTEM image (Fig. 3d), indicating that the nitride multilayers have a better microstructural stability than the metallic multilayers under irradiation at RT. The SAED pattern (Fig. 3d) acquired in the unirradiated region (right bottom, from the circled area 3) consists of two sets of *fcc*-phase diffraction spots. Both TiNbZrTaN and CrFeCoNiN$_x$ sublayers form an *fcc* phase structure (referred to *fcc2* and *fcc3* in XRD patterns, Fig. 2c and d). After irradiation, however, the TiNbZrTaN sublayers can remain crystalline but more random-oriented (Fig. 3d, insets), while CrFeCoNiN$_x$ sublayers turn into amorphous (Fig. 3f). These observations indicate that the TiNbZrTaN sublayers has a better structural stability compared to the CrFeCoNiN$_x$ sublayers under irradiation at RT.

3.3. Microstructural characterization of the metallic and nitride multilayers irradiated at 500 °C

Fig. 4 shows the microstructural evolution for metallic and nitride multilayers irradiated at 500 °C, respectively. In the case of the metallic multilayer which was irradiated at 500 °C, the period multilayer feature disappears in the irradiation region but remained in the unirradiated region as shown in Fig. 4a. The SAED pattern from the unirradiated region (circled area 1) consists of a series of bright spots together with a weak amorphous ring. The bilayer thickness maintained around 28 nm after annealing (Fig. 4b), however within the bilayer, the CrFeCoNi sublayer thickness decreases to 8 nm compared to 11 nm in the pristine film (Fig. 3b) and the TiNbZrTa sublayer thickness increases from 17 to 20 nm. The corresponding FFT patterns show that the CrFeCoNi sublayers maintain their crystallinity while TiNbZrTa sublayers are amorphous. These microstructural change of sublayers in metallic multilayers which result from the constituent element diffusion at high temperature will be discussed in the following section. After irradiation by Xe-ions, the multilayer periods (Fig. 4c) and crystallinity of the metallic multilayer films disappeared, as shown in SAED pattern (right up, Fig. 4a) and the FFT pattern (right up, Fig. 4c). It indicates that the microstructure of metallic multilayer is unstable after either annealing at 500 °C or irradiation.

For the nitride multilayers irradiated at 500 °C, distinct multilayer periods for both irradiated and unirradiated areas can be observed in a low-magnification BFTEM image (Fig. 4d). The SAED pattern taken from the unirradiated area is composed of two-set diffraction spots corresponding to the *fcc* phases (*i.e.*, *fcc2* and *fcc3* in XRD patterns, Fig. 2c and d), while the SAED pattern from the irradiated area shows continuous arcs. These observations suggest that the textured grains are refined after irradiation but maintain the same *fcc* structures as the unirradiated area. Details of the
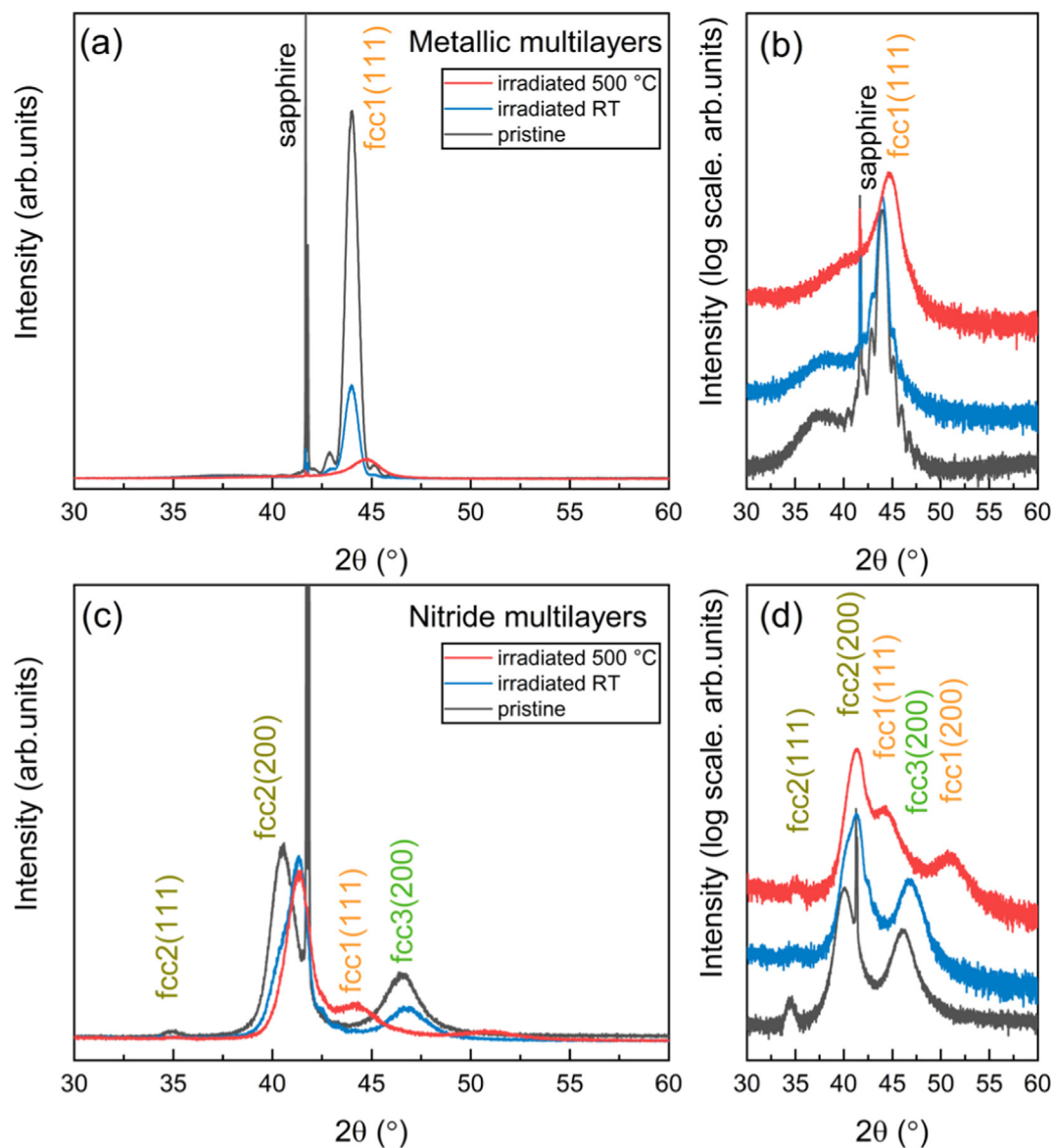
Fig. 2. (a) θ-2θ X-ray diffractograms of the TiNbZrTa/CrFeCoNi metallic multilayers on c-sapphire substrates, before and after irradiated at RT, and 500 °C, respectively. (b) is the zoomed diffractogram plotted in log scale from 30° to 60°. (c) θ-2θ X-ray diffractograms of the TiNbZrTa/CrFeCoNi nitride multilayers on c-sapphire substrates, before and after irradiated at RT, and 500 °C, respectively. (d) is the zoomed in diffractogram plotted in log scale from 30° to 60°.

microstructural evolution is revealed by HRTEM images and FFT patterns from the unirradiated (Fig. 4e) and irradiated area (Fig. 4f). Both CrFeCoNiN$_x$ sublayers and TiNbZrTaN sublayers have a 200-textured *fcc* phase structure in the unirradiated areas, and no phase transformations are found compared to the unirradiated area at RT (Fig. 3e). The crystal structure is retained after irradiation, although the intensity becomes weak (FFT patterns, Fig. 4f). The nitride multilayers possess a better structural stability than the metallic multilayers at 500 °C and Xe-ion irradiation conditions.

3.4. Element segregation

To further understand the microstructural evolution of both metallic and nitride multilayers under Xe-ion irradiation at different temperature, EDX elemental mappings of constituent elements from unirradiated and irradiated areas are provided (Fig. 5). At RT, Fig. 5a and c show the elemental mappings acquired from the unirradiated areas for metallic and nitride multilayer, respectively. The intermittent interfaces of each mapping in the sublayers indicate the multilayer periods for both metallic and nitrides in as-deposited films. The elemental distribution in irradiated region of the metallic multilayers (Fig. 5b) shows a significant change. All the constituent elements except for Cr and Fe tend to distribute homogeneously. Whereas all the metal elements in the irradiated nitride multilayers in Fig. 5d are retained in the individual sublayers as seen in the pristine multilayers (Fig. 5c). Note that stronger intensity signals of nitrogen detected in TiNbZrTa sublayers compared to CrFeCoNi sublayers is due to the fact that the refractory metals have a stronger nitride formation ability [24,39], this is also consistent with measured nitrogen content of 50 at.% and 18 at.% in the individual TiNbZrTaN and CrFeCoNiN nitride films, respectively (see Fig. S1). The above results suggest that the nitride multilayers have higher microstructural stability under RT irradiation condition in comparison to the metallic multilayers and the addition of N can reduce element diffusion.

Heat treatment typically promotes elemental diffusion. A significantly different elemental mapping can be observed in TiNbZrTa/
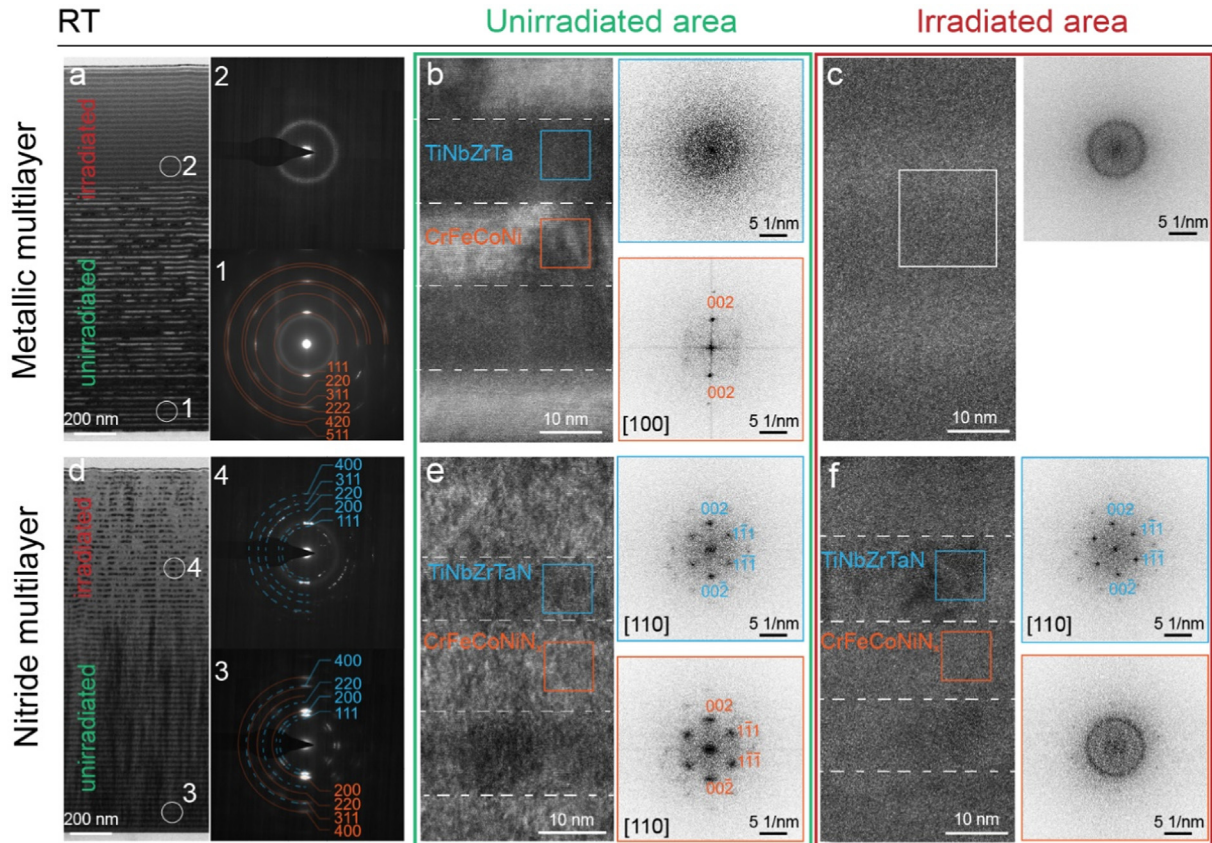
Fig. 3. Comparison of microstructural evolution along the growth direction between TiNbZrTa/CrFeCoNi metallic and nitride multilayer under Xe-ion irradiation at RT. (a) Overview BFTEM image for metallic multilayer, inserts 1 and 2 are SAED patterns acquired from unirradiated and irradiated areas, respectively. (b) and (c) HRTEM images acquired at unirradiated and irradiated areas, respectively. Insets in b and c are FFT patterns of the boxed area in corresponding TiNbZrTa and CrFeCoNi sublayers, respectively. (d) Overview BFTEM image for nitride multilayer, insets 3 and 4 are SAED patterns acquired from unirradiated and irradiated areas, respectively. (e) and (f) HRTEM images acquired at unirradiated and irradiated areas. Insets in e and f are FFT patterns of the boxed area in corresponding TiNbZrTa and CrFeCoNi sublayers, respectively.

CrFeCoNi metallic multilayers after being irradiated at 500 °C (Fig. 6a and b). For the unirradiated area, Co and Ni diffused mutually between the TiNbZrTa and CrFeCoNi layers to a much larger extent in comparison to Cr and Fe which remained in place. Intriguingly, Ni is found to mix with Ti, Zr, Nb and Ta elements (*i.e.*, in the TiNbZrTa sublayers), whereas Co and Ti mixed homogeneously in entire film. It indicates that annealing treatment promoted the atomic mixing of Co, Ni and Ti elements, and they can easily diffuse over the interfacial barriers at 500 °C. Nb, Zr, Ta, Fe and Cr preferred to stay in their own previous sublayers. This elemental diffusion is associated with the thickness changes of both sublayers observed in the corresponding HRTEM images (Fig. 4b and 6b). Fig. 6b shows an interfacial region between irradiated and unirradiated metallic multilayers along the growth direction. On top of Fig. 6b, all the constituent eight elements are homogeneously distributed in irradiated area, and no multilayer periods are detected, which indicates the irradiation further enhanced the elemental diffusion and atomic mixing. Fig. 6c and d show the elemental mappings corresponding to the constituents for the nitride multilayers after being irradiated at 500 °C. All the elements were retained in their own sublayers for both unirradiated and irradiated areas. No observable diffusion or mixing could be found.

4. Discussion

4.1. Element segregation in the metallic and nitride multilayers

As the most commonly studied HEA system, CrFeCoNi-based Cantor alloys [19] show a special sluggish diffusion behavior and a decreasing diffusion rate in the sequence of Cr, Fe, Co and Ni [40]. Barr et al. [41] reported that in the CrFeCoNiMn HEA, the elements Mn and Cr with higher diffusion rates tend to deplete, while the elements Co and Ni with slower diffusion rates prefer to aggregate at grain boundaries (GBs). Similar observations of element segregation behavior and its relationship with the diffusion coefficients have also been reported in other CrFeCoNi -based HEAs and conventional alloys [42–44], and the relationship is well established by the inverse Kirkendall model [43,44]. In this study, Co and Ni in CrFeCoNi sublayer of the metallic multilayers were observed to diffuse into the adjacent TiNbZrTa sublayers across the interfacial barriers, and Ti element was found to diffuse into the adjacent CrFeCoNi sublayer and distribute relatively homogeneously in the multilayers after annealing at 500 °C for 2.5 h without irradiation, while Cr, Fe, Ta, Zr and Nb preferred to stay within their own sublayers (as shown in Fig. 6a, Table S1, and Fig. S1).

Moreover, a similar diffusion trend between CrCoNi and TiZrNbHf sublayers in CrCoNi/TiZrNbHf multilayer system was reported in a very recent study [45], Cr retained at the parent layer when annealed at 700 °C, but Co and Ni diffused and mixed with adjacent TiZrNbHf sublayers.

Due to the random distribution of constituent metal atoms in the amorphous phase, there may be a higher number of vacancies present in the TiNbZrTa sublayer [46–48]. The CrFeCoNi sublayers have a nanocrystalline microstructure with a relatively less vacancies concentration. Therefore, the vacancy-rich TiNbZrTa sublayers act as defect sinks in the metallic multilayer system and an obvious vacancy concentration gradient formed near the adjacent two sublayers. During the heat treatment at 500 °C, diffusion fluxes of vacancies from the amorphous TiNbZrTa sublayers to nanocrystalline CrFeCoNi sublayers are predominant. Based on the inverse Kirkendall model, the fastest vacancy-diffuser elements (*i.e.*, Cr and Fe) should migrate reversely along the direction of vacancies, leading to a depletion, and the slowest vacancy-diffuser elements (*i.e.*, Co and Ni) enrich at the defect sinks. However, an opposite trend was observed in this study, *i.e.*, Cr and Fe remained in the CrFeCoNi sublayers while Co and Ni diffused into TiNbZrTa sublayers. This result indicated that the inverse Kirkendall model, although applicable for alloys of the late 3d transition metals, cannot be directly applied when considering the broader range of transition metals and complex structures.

Literature suggests that the difference in atomic sizes between the constituent elements plays an important role in the element segregation behavior in HEAs [49,50], and the same can explain the diffusion behavior of Cr, Fe, Co, and Ni elements in the metallic

multilayers [49]. As discussed in above, the random distribution of Ti, Nb, Zr, and Ta atoms leads to abundant vacancy sites. Therefore, it is energetic favorable for the small-size atoms (Co and Ni) rather than the large-size atoms (Fe and Cr) to migrate across the interface and occupy the vacant spaces. In this study, Co and Ni with smaller atomic size (1.253 and 1.246 Å, respectively. [51]) are prone to diffuse compared to Cr and Fe with larger atomic size (1.271 and 1.282 Å, respectively.). On the other hand, the atomic sizes of Ti (1.462 Å), Nb (1.468 Å), Zr (1.602 Å), and Ta (1.467 Å) are all larger than all the elements from the CrFeCoNi sublayers. It is therefore energetically unfavorable for them to diffuse into the CrFeCoNi sublayers. However, Ti is an exception, indicating that the atomic size is not the sole factor responsible for the segregation behavior.

To further understand the underlying reasons, we calculated the typical empirical parameters of HEAs, configurational entropy (ΔS_{conf}, [18]), and mixing enthalpy (ΔH_{mix}, [52]) for the possible diffusion product systems TiNbZrTaX (X = Cr, Fe, Co, Ni) in equiatomic composition, and listed in Table 1. It shows that ΔH_{mix} of TiNbZrTaX systems decreased in the order of Cr, Fe, Co, and Ni, whereas ΔS_{conf} was constant in equiatomic quinary systems. Therefore, the alloy systems with a lower ΔH_{mix} possesses a lower Gibbs free energy and are more stable from a thermodynamic point of view. The thermodynamic stability of these four systems decreases in order of TiNbZrTaNi (-21.28 kJ/mol), TiNbZrTaCo (-17.28 kJ/mol), TiNbZrTaFe (-10.08 kJ/mol), and TiNbZrTaCr (-3.68 kJ/mol), suggesting that the diffusion of Ni and Co into TiNbZrTa sublayers are more energetically favorable for the entire multilayer systems. This trend is also consistent with our experi-
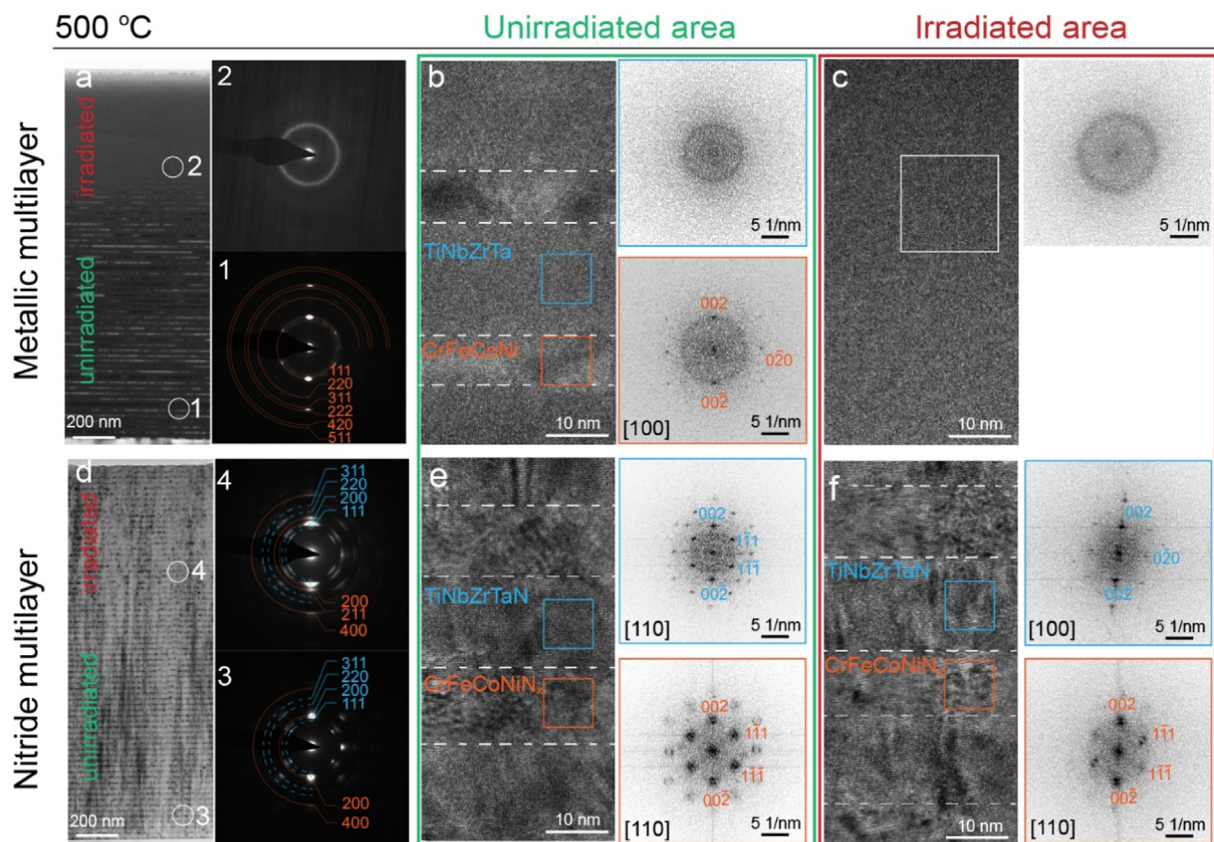

Fig. 4. Comparison of microstructural evolution between TiNbZrTa/CrFeCoNi metallic and nitride multilayer under Xe ions irradiation at 500 °C. (a) Overview BFTEM image for metallic multilayer, inset 1 and 2 are SAED patterns taken in sequence from unirradiated and irradiated areas. (b) and (c) HRTEM images acquired at unirradiated and irradiatied areas. Insets in b and c are FFT patterns of the boxed area in corresponding TiNbZrTa and CrFeCoNi sublayers. (d) Overview BFTEM image for nitride multilayer, inset 3 and 4 are SAED patterns acquired from unirradiated and irradiated areas, respectively. (e) and (f) are HRTEM images acquired in unirradiated and irradiatied areas. Insets in e and f are FFT patterns of the boxed area in corresponding TiNbZrTa and CrFeCoNi sublayers.
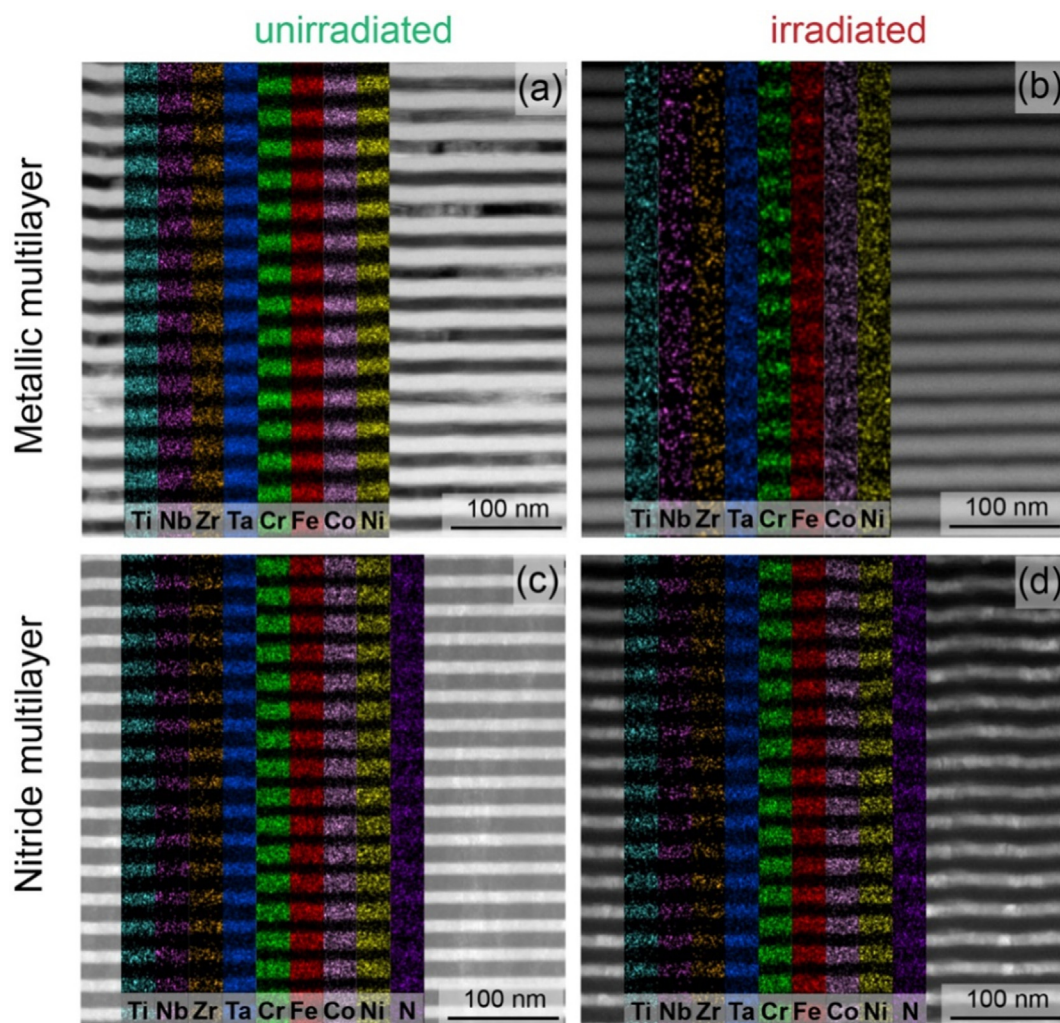
Fig. 5. Elemental mappings corresponding to Ti, Nb, Zr, Ta, Cr, Fe, Co, and Ni elements, for the TiNbZrTa/CrFeCoNi metallic multilayers: unirradiated area (a) and irradiated area (b) at RT condition; Elemental mappings corresponding to Ti, Nb, Zr, Ta, Cr, Fe, Co, Ni and N elements, for the TiNbZrTa/CrFeCoNi nitride multilayers: unirradiated area (c) and irradiated area (d) at RT condition.

mental observations. Furthermore, values of mixing enthalpy of the atomic pairs between the constituent elements of the multilayers are presented in Table S2 [52]. It clearly shows that the mixing enthalpy of Ti and Zr with individual constituent element of CrFeCoNi sublayers are lower than that of the Nb and Ta elements, which indicate that Ti and Zr are more energetically preferred to mix with CrFeCoNi sublayers. However, the size of Zr atoms is exceptionally larger than the Ti atoms, which inhibits the diffusion of Zr into CrFeCoNi sublayers. Overall, the elements segregation behavior in the multilayer systems depends on both the atomic size difference and enthalpy of mixing between the constituent elements.

For the as-deposited nitride multilayers, the nitrogen content in TiNbZrTa sublayer is overstoichiometric ($\sim$56 at.%), and much more than that of $\sim$ 23 at.% in CrFeCoNi sublayer (see Fig. S1), even deposited at the same nitrogen flow ratio. This is mainly due to the fact that refractory metals (Ti, Zr, Nb and Ta) typically have stronger nitride formation abilities compared to the transition metals (Cr, Fe, Ni and Co), the latter three are almost non-nitride formers[24,39]. For diffusion to occur between the CrFeCoNiN$_x$ sublayer and the TiNbZrTaN sublayer, the element Me in the sublayers need to overcome a high energy threshold to break the strong Me-N bond (Me being a nitride forming metal), and diffusion energy barrier. The stable Me-N bonding in TiNbZrTaN multilayers will pre-

vent the elements in CrFeCoNiN$_x$ sublayers from diffusing across interfaces between two sublayers. The CrN-type nitride (*fcc*3 phase) also stabilize the CrFeCoNiN$_x$ sublayers at room temperature. Therefore, the formation of a stable nitride in sublayers prevents the whole system from collapsing by lowering the energy state and results in a structurally stable multilayer system.

4.2. Microstructural evolution of the metallic multilayers under irradiation condition

Regarding the response for irradiation to the metallic multilayers, the *fcc* phase structure in pristine CrFeCoNi sublayers was destroyed and transformed into amorphous, along with atomic mixing between CrFeCoNi and TiNbZrTa sublayers, especially in the area near the highest displacement damage. Considering that the ions induced displacement damage was near 13.3 dpa at the peak damage region, such a distinct microstructural evolution of CrFeCoNi sublayers in this work is different with the reported high structural stability of CrFeCoNi-based HEAs against irradiation [53,54]. This difference originates from the nonuniformity of microstructures (*i.e.*, coexistence of crystal CrFeCoNi sublayers and amorphous TiNbZrTa sublayers) and the incompatibility of mixing elements. In detail, energetic ions bombardment induced a series of atomic collision cascades. In the collision cascade
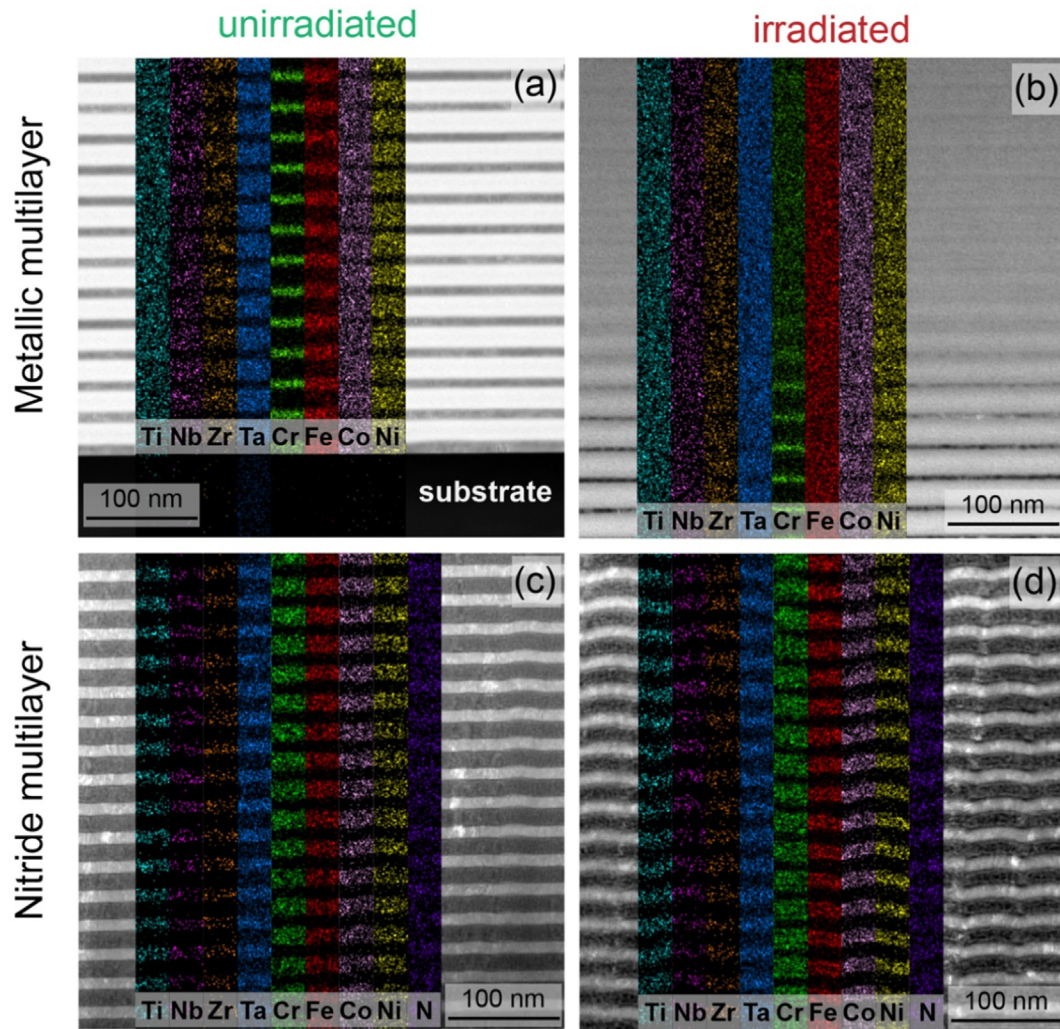
Fig. 6. Elemental mappings corresponding to Ti, Nb, Zr, Ta, Cr, Fe, Co, and Ni elements, for the TiNbZrTa/CrFeCoNi metallic multilayers: unirradiated area (a) and irradiated area on top of (b) at 500 °C; Elemental mappings corresponding to Ti, Nb, Zr, Ta, Cr, Fe, Co, Ni and N elements, for the TiNbZrTa/CrFeCoNi nitride multilayers: unirradiated area (c) and irradiated area (d) at 500 °C.

Table 1
Calculated configurational entropy changes ($\Delta S_{conf.}$) and enthalpy changes (ΔH_{mix}) of TiNbZrTa system mixed with Cr, Fe, Co, and Ni elements.

Composition	$\Delta S_{conf.}$ ($JK^{-1}mol^{-1}$)	$\Delta H_{mix.}$ ($kJmol^{-1}$)
TiNbZrTa	11.53	2.50
TiNbZrTaCr	13.38	−3.68
TiNbZrTaFe	13.38	−10.08
TiNbZrTaCo	13.38	−17.28
TiNbZrTaNi	13.38	−21.28

regions near the interface of adjacent sublayers, the displaced atoms of crystalline CrFeCoNi sublayers mix with the atoms of amorphous TiNbZrTa sublayers (ion beam mixing effects) [55]. During this dynamic process, numerous interstitials and vacancies were created, although more than 99% of them are annihilated by recombination [56], it is still far from equilibrium. As a result, the incompatible atoms from two different groups of HEAs makes it harder to restore the former *fcc* crystalline structure [57], and results in an amorphous state. Therefore, the disordered interface between the adjacent sublayers provide nucleation sites for the growing amorphous phase [58]. Similar crystal-to-amorphous transition process was also identified in SiC, Fe/Cu multilayers

and Y/Zr multilayers under irradiation condition [59–61]. Although many experimental observations are consistent with this hypothesis, a series of further experimental and theoretical data is required to verify it.

4.3. Microstructural evolution of the nitride multilayers under irradiation condition

Compared to the TiNbZrTa/CrFeCoNi metallic multilayers, the nitride multilayers with the same constituent metal elements show a better structural stability and resistance to element segregation under irradiation at 500 °C. As shown in Fig. 3 and Fig. 4, the microstructural features of the nitride multilayers revealed by HRTEM and SAED patterns after irradiation at 500 °C remain the same as the as-deposition condition. Moreover, no metal elements were found to diffuse between the sublayers. This is obviously different with the amorphous and homogenous atomic mixing feature in the metallic multilayers irradiated at the same condition. It proves that the addition of N element promotes the structural stability of both the CrFeCoNi and TiNbZrTa sublayers against amorphization and elemental diffusion at high temperature irradiation.

The above-mentioned preferential chemical affinity of N elements with certain principal metal elements [24,39] leads to a prioritized enrichment of elements in the sequence of Ti, Zr, Ta and Nb around N elements in the TiNbZrTaN sublayers and in the sequence of Cr, Fe, Co, and Ni elements in the CrFeCoNi sublayers. The chemical affinity results in an atomic-level compositional heterogeneity [62]. Furthermore, recent studies reported that the lattice distortion of multicomponent solid solution materials originated from the preferential bonding between constituent elements pairs rather than from the atomic size mismatch effect [63,64]. It means that the bigger difference of affinity between N element and constituent elements results in a higher degree of lattice distortion. The significant atomic-level heterogeneity of chemical composition and lattice distortion result in complex energy landscapes [23], and enhance radiation induced point defects combination by constraining motion path of defects and slowing down the interdiffusion of radiation induced interstitials [53]. These properties improve irradiation resistance of both the CrFeCoNiN$_x$ and TiNbZrTaN sublayers.

5. Conclusion

High-entropy TiNbZrTa/CrFeCoNi metallic and nitride multilayers with bilayer thickness of 30 nm were synthesized on Al$_2$O$_3$(0001) by magnetron sputtering to a total thickness of $\sim$ 2 μm. The films were irradiated by 3-MeV Xe ions to a fluence of 2×10^{15} ions/cm^2 at RT and 500 °C, respectively. A comparison of metallic multilayers and its counterpart nitride multilayers proves that addition of nitrogen increases both high temperature stability and irradiation resistance. The outcomes in this work thus provide a design strategy of high-entropy nitride for nuclear fuel cladding.

The crystallinity of TiNbZrTa/CrFeCoNi metallic multilayers deteriorated either at high temperature or under irradiation conditions, while the crystal structure of nitride multilayers was retained after the same conditions. Moreover, the evaluated temperature of 500 °C caused a significant element segregation in the metallic multilayers. Ni and Co preferred to diffuse into the adjacent TiNbZrTa sublayers, Ti was detected to be homogeneously distributed in the multilayer system, whereas no obvious diffusion for the rest elements is detected.

No detectable element segregation happened for the nitride multilayers after irradiation at RT and 500 °C. The structural and chemical stability of the nitride multilayer system under both high temperature and irradiation condition were attributed to a stronger chemical affinity of N element with the constitutional metal elements and the low Gibbs free energy of the system.

CRediT authorship contribution statement

Ji Wang: Conceptualization, Investigation, Data curation, Formal analysis, Writing - original draft, Funding acquisition. **Rui Shu:** Conceptualization, Investigation, Data curation, Formal analysis, Writing - original & editing. **Jianlong Chai:** Investigation, Formal analysis. **Smita G. Rao:** Investigation, Formal analysis, review & editing, Writing - review & editing. **Arnaud le Febvrier:** Investigation, Supervision, Formal analysis, Writing - review & editing. **Haichen Wu:** Investigation, Formal analysis. **Yabin Zhu:** Investigation, Formal analysis. **Cunfeng Yao:** Investigation, Formal analysis. **Laihui Luo:** Investigation, Formal analysis. **Weiping Li:** Investigation, Formal analysis. **Peifeng Gao:** Supervision, Writing - review & editing, Funding acquisition. **Per Eklund:** Project administration, Conceptualization, Supervision, Writing - review & editing, Funding acquisition.

Data availability

The data that support these findings are available from the corresponding author on request.

Declaration of Competing Interest

The authors declare that they have no known competing financial interests or personal relationships that could have appeared to influence the work reported in this paper.

Appendix A. Supplementary material

Supplementary data to this article can be found online at https://doi.org/10.1016/j.matdes.2022.110749.

References

[1] K.A. Terrani, Accident tolerant fuel cladding development: Promise, status, and challenges, J. Nucl. Mater. 501 (2018) 13–30, https://doi.org/10.1016/j.jnucmat.2017.12.043.

[2] S.J. Zinkle, K.A. Terrani, J.C. Gehin, L.J. Ott, L.L. Snead, Accident tolerant fuels for LWRs: A perspective, J. Nucl. Mater. 448 (2014) 374–379, https://doi.org/10.1016/j.jnucmat.2013.12.005.

[3] S.J. Zinkle, G.S. Was, Materials challenges in nuclear energy, Acta Mater. 61 (2013) 735–758, https://doi.org/10.1016/j.actamat.2012.11.004.

[4] Z. Zhang, D.E.J. Armstrong, P.S. Grant, The effects of irradiation on CrMnFeCoNi high-entropy alloy and its derivatives, Prog. Mater. Sci. 123 (2022) 100807. https://doi.org/10/gm5f36.

[5] M.A. Tunes, V.M. Vishnyakov, S.E. Donnelly, Synthesis and characterisation of high-entropy alloy thin films as candidates for coating nuclear fuel cladding alloys, Thin Solid Films 649 (2018) 115–120, https://doi.org/10.1016/j.tsf.2018.01.041.

[6] F. Wang, X. Yan, T. Wang, Y. Wu, L. Shao, M. Nastasi, Y. Lu, B. Cui, Irradiation damage in (Zr$_{0.25}$Ta$_{0.25}$Nb$_{0.25}$Ti$_{0.25}$)C high-entropy carbide ceramics, Acta Mater. 195 (2020) 739–749. https://doi.org/10.1016/j.actamat.2020.06.011.

[7] A.D. Pogrebnjak, I.V. Yakushchenko, O.V. Bondar, V.M. Beresnev, K. Oyoshi, O. M. Ivasishin, H. Amekura, Y. Takeda, M. Opielak, C. Kozak, Irradiation resistance, microstructure and mechanical properties of nanostructured (TiZrHfVNbTa)N coatings, J. Alloys Compd. 679 (2016) 155–163, https://doi.org/10.1016/j.jallcom.2016.04.064.

[8] F.F. Komarov, A.D. Pogrebnyak, S.V. Konstantinov, Radiation resistance of high-entropy nanostructured (Ti, Hf, Zr, V, Nb)N coatings, Tech. Phys. 60 (2015) 1519–1524, https://doi.org/10.1134/S1063784215100187.

[9] M.J. Demkowicz, R.G. Hoagland, J.P. Hirth, Interface structure and radiation damage resistance in Cu-Nb multilayer nanocomposites, Phys. Rev. Lett. 100 (2008), https://doi.org/10.1103/PhysRevLett.100.136102 136102.

[10] J. Marfaing, W. Marine, B. Vidal, M. Toulemonde, M. Hage Ali, J.P. Stoquert, Crystallization of ultrathin W-Si multilayer structures by high-energy heavy ion irradiations, Appl. Phys. Lett. 57 (1990) 1739–1741, https://doi.org/10.1063/1.104052.

[11] X.Q. Liang, J.Y. Zhang, Y.Q. Wang, S.H. Wu, F. Zeng, K. Wu, G. Liu, G.J. Zhang, J. Sun, Tuning the size-dependent He-irradiated tolerance and strengthening

behavior of crystalline/amorphous Cu/Ta nanostructured multilayers, Mater. Sci. Eng. A. 672 (2016) 153–160, https://doi.org/10.1016/j.msea.2016.07.005.

[12] L.F. Zhang, R. Gao, J. Hou, L.F. Zeng, J.J. Xin, X.B. Wu, X.P. Wang, Q.F. Fang, C.S. Liu, The effects of interfaces stability on mechanical properties, thermal conductivity and helium irradiation of V/Cu nano-multilayer composite, Mater. Des. 216 (2022), https://doi.org/10.1016/j.matdes.2022.110535 110535.

[13] M. Wang, I.J. Beyerlein, J. Zhang, W.Z. Han, Defect-interface interactions in irradiated Cu/Ag nanocomposites, Acta Mater. 160 (2018) 211–223, https://doi.org/10.1016/j.actamat.2018.09.003.

[14] K.Y. Yu, Y. Liu, E.G. Fu, Y.Q. Wang, M.T. Myers, H. Wang, L. Shao, X. Zhang, Comparisons of radiation damage in He ion and proton irradiated immiscible Ag/Ni nanolayers, J. Nucl. Mater. 440 (2013) 310–318, https://doi.org/10.1016/j.jnucmat.2013.04.069.

[15] A.D. Pogrebnjak, R.F. Webster, R.D. Tilley, V.V. Buranich, V.I. Ivashchenko, Y. Takeda, K. Oyoshi, R. Sakenova, K. Piotrowska, P. Zukowski, P. Konarski, A.I. Kupchishin, P. Budzynski, Formation of Si-rich interfaces by radiation-induced diffusion and microsegregation in CrN/ZrN nanolayer coating, ACS Appl. Mater. Interfaces. 13 (2021) 16928–16938, https://doi.org/10.1021/acsami.0c19451.

[16] N. Li, E.G. Fu, H. Wang, J.J. Carter, L. Shao, S.A. Maloy, A. Misra, X. Zhang, He ion irradiation damage in Fe/W nanolayer films, J. Nucl. Mater. 389 (2009) 233–238, https://doi.org/10.1016/j.jnucmat.2009.02.007.

[17] M. Milosavljević, A. Grce, D. Peruško, M. Stojanović, J. Kovač, G. Dražič, A.Y. Didyk, V.A. Skuratov, A comparison of Ar ion implantation and swift heavy Xe ion irradiation effects on immiscible AlN/TiN multilayered nanostructures, Mater. Chem. Phys. 133 (2012) 884–892, https://doi.org/10.1016/j.matchemphys.2012.01.112.

[18] J.W. Yeh, S.K. Chen, S.J. Lin, J.Y. Gan, T.S. Chin, T.T. Shun, C.H. Tsau, S.Y. Chang, Nanostructured high-entropy alloys with multiple principal elements: novel alloy design concepts and outcomes, Adv. Eng. Mater. 6 (2004) 299–303, https://doi.org/10.1002/adem.200300567.

[19] B. Cantor, I.T.H. Chang, P. Knight, A.J.B. Vincent, Microstructural development in equiatomic multicomponent alloys, Mater. Sci. Eng. A. 375–377 (2004) 213–218, https://doi.org/10.1016/j.msea.2003.10.257.

[20] O.N. Senkov, D.B. Miracle, K.J. Chaput, J.-P. Couzinie, Development and exploration of refractory high entropy alloys—A review, J. Mater. Res. 33 (2018) 1–37, https://doi.org/10.1557/jmr.2018.153.

[21] T. Egami, W. Guo, P.D. Rack, T. Nagase, Irradiation resistance of multicomponent alloys, Metall. Mater. Trans. A. 45 (2014) 180–183, https://doi.org/10.1007/s11661-013-1994-2.

[22] B. Kombaiah, K. Jin, H. Bei, P.D. Edmondson, Y. Zhang, Phase stability of single phase Al0.12CrNiFeCo high entropy alloy upon irradiation, Mater. Des. 160 (2018) 1208–1216, https://doi.org/10.1016/j.matdes.2018.11.006.

[23] Z. Su, J. Ding, M. Song, L. Jiang, T. Shi, Z. Li, S. Wang, F. Gao, D. Yun, C. Lu, E. Ma, Radiation-tolerant high-entropy alloys via interstitial-solute-induced chemical heterogeneities, ArXiv Prepr. ArXiv. (2021). http://arxiv.org/abs/2103.15134 (accessed September 6, 2021).

[24] E. Lewin, Multi-component and high-entropy nitride coatings—A promising field in need of a novel approach, J. Appl. Phys. 127 (16) (2020) 160901, https://doi.org/10.1063/1.5144154.

[25] A.D. Pogrebnjak, I.V. Yakushchenko, A.A. Bagdasaryan, O.V. Bondar, R. Krause-Rehberg, G. Abadias, P. Chartier, K. Oyoshi, Y. Takeda, V.M. Beresnev, O.V. Sobol, Microstructure, physical and chemical properties of nanostructured (Ti–Hf–Zr–V–Nb)N coatings under different deposition conditions, Mater. Chem. Phys. 147 (2014) 1079–1091, https://doi.org/10.1016/j.matchemphys.2014.06.062.

[26] A. Kirnbauer, A. Kretschmer, C.M. Koller, T. Wojcik, V. Paneta, M. Hans, J.M. Schneider, P. Polcik, P.H. Mayrhofer, Mechanical properties and thermal stability of reactively sputtered multi-principal-metal Hf-Ta-Ti-V-Zr nitrides, Surf. Coat. Technol. 389 (2020), https://doi.org/10.1016/j.surfcoat.2020.125674 125674.

[27] M.H. Tsai, C.W. Wang, C.H. Lai, J.W. Yeh, J.Y. Gan, Thermally stable amorphous (AlMoNbSiTaTiVZr)50N50 nitride film as diffusion barrier in copper metallization, Appl. Phys. Lett. 92 (5) (2008) 052109, https://doi.org/10.1063/1.2841810.

[28] R. Shu, E.-M. Paschalidou, S.G. Rao, B. Bakhit, R. Boyd, M.V. Moro, D. Primetzhofer, G. Greczynski, L. Nyholm, A. le Febvrier, P. Eklund, Effect of nitrogen content on microstructure and corrosion resistance of sputter-deposited multicomponent (TiNbZrTa)Nx films, Surf. Coat. Technol. 404 (2020), https://doi.org/10.1016/j.surfcoat.2020.126485 126485.

[29] A.D. Pogrebnjak, A.A. Bagdasaryan, P. Horodek, V. Tarelnyk, V.V. Buranich, H. Amekura, N. Okubo, N. Ishikawa, V.M. Beresnev, Positron annihilation studies of defect structure of (TiZrHfNbV)N nitride coatings under Xe14+ 200 MeV ion irradiation, Mater. Lett. 303 (2021) 130548, https://doi.org/10.1016/j.matlet.2021.130548.

[30] A. le Febvrier, L. Landälv, T. Liersch, D. Sandmark, P. Sandström, P. Eklund, An upgraded ultra-high vacuum magnetron-sputtering system for high-versatility and software-controlled deposition, Vacuum 187 (2021), https://doi.org/10.1016/j.vacuum.2021.110137 110137.

[31] M.V. Moro, R. Holeňák, L. Zendejas Medina, U. Jansson, D. Primetzhofer, Accurate high-resolution depth profiling of magnetron sputtered transition metal alloy films containing light species: A multi-method approach, Thin Solid Films 686 (2019) https://doi.org/10.1016/j.tsf.2019.137416 137416.

[32] K. Arstila, J. Julin, M.I. Laitinen, J. Aalto, T. Konu, S. Kärkkäinen, S. Rahkonen, M. Raunio, J. Itkonen, J.P. Santanen, T. Tuovinen, T. Sajavaara, Potku – New analysis software for heavy ion elastic recoil detection analysis, Nucl. Instrum.

[33] M. to Baben, M. Hans, D. Primetzhofer, S. Evertz, H. Ruess, J.M. Schneider, Unprecedented thermal stability of inherently metastable titanium aluminum nitride by point defect engineering, Mater. Res. Lett. 5 (3) (2017) 158–169, https://doi.org/10.1080/21663831.2016.1233914.

[34] J.F. Ziegler, M.D. Ziegler, J.P. Biersack, SRIM – The stopping and range of ions in matter (2010), Nucl. Instrum. Methods Phys. Res., Sect. B 268 (11–12) (2010) 1818–1823, https://doi.org/10.1016/j.nimb.2010.02.091.

[35] H. Söderberg, M. Odén, J. Flink, J. Birch, P.O.Å. Persson, M. Beckers, L. Hultman, Growth and characterization of TiN/SiN(001) superlattice films, J. Mater. Res. 22 (2007) 3255–3264, https://doi.org/10.1557/JMR.2007.0412.

[36] S. Bagchi, F. Singh, D.K. Avasthi, N.P. Lalla, Thickness dependent effect of swift heavy ion irradiation in W/Ni superlattice multilayers, J. Phys. Appl. Phys. 42 (14) (2009) 145414, https://doi.org/10.1088/0022-3727/42/14/145414.

[37] Y. Gao, T. Yang, J. Xue, S. Yan, S. Zhou, Y. Wang, D.T.K. Kwok, P.K. Chu, Y. Zhang, Radiation tolerance of Cu/W multilayered nanocomposites, J. Nucl. Mater. 413 (2011) 11–15, https://doi.org/10.1016/j.jnucmat.2011.03.030.

[38] P.D. Edmondson, C.M. Parish, Y. Zhang, A. Hallén, M.K. Miller, Helium bubble distributions in a nanostructured ferritic alloy, J. Nucl. Mater. 434 (2013) 210–216, https://doi.org/10.1016/j.jnucmat.2012.11.049.

[39] R. Shu, D. Lundin, B. Xin, M.A. Sortica, D. Primetzhofer, M. Magnuson, A. le Febvrier, P. Eklund, Influence of metal substitution and ion energy on microstructure evolution of high-entropy nitride (TiZrTaMe)N1−x (Me = Hf, Nb, Mo, or Cr) films, ACS Appl. Electron. Mater. 3 (2021) 2748–2756, https://doi.org/10.1021/acsaelm.1c00311.

[40] K.Y. Tsai, M.H. Tsai, J.W. Yeh, Sluggish diffusion in Co–Cr–Fe–Mn–Ni high-entropy alloys, Acta Mater. 61 (2013) 4887–4897, https://doi.org/10.1016/j.actamat.2013.04.058.

[41] C.M. Barr, J.E. Nathaniel, K.A. Unocic, J. Liu, Y. Zhang, Y. Wang, M.L. Taheri, Exploring radiation induced segregation mechanisms at grain boundaries in equiatomic CoCrFeNiMn high entropy alloy under heavy ion irradiation, Scr. Mater. 156 (2018) 80–84, https://doi.org/10.1016/j.scriptamat.2018.06.041.

[42] C. Lu, T. Yang, K. Jin, N. Gao, P. Xiu, Y. Zhang, F. Gao, H. Bei, W.J. Weber, K. Sun, Y. Dong, L. Wang, Radiation-induced segregation on defect clusters in single-phase concentrated solid-solution alloys, Acta Mater. 127 (2017) 98–107, https://doi.org/10.1016/j.actamat.2017.01.019.

[43] J.P. Wharry, G.S. Was, The mechanism of radiation-induced segregation in ferritic–martensitic alloys, Acta Mater. 65 (2014) 42–55, https://doi.org/10.1016/j.actamat.2013.09.049.

[44] J.P. Wharry, Z. Jiao, G.S. Was, Application of the inverse Kirkendall model of radiation-induced segregation to ferritic–martensitic alloys, J. Nucl. Mater. 425 (2012) 117–124, https://doi.org/10.1016/j.jnucmat.2011.10.035.

[45] G. Wu, C. Liu, A. Brognara, M. Ghidelli, Y. Bao, S. Liu, X. Wu, W. Xia, H. Zhao, J. Rao, D. Ponge, V. Devulapalli, W. Lu, G. Dehm, D. Raabe, Z. Li, Symbiotic crystal-glass alloys via dynamic chemical partitioning, Mater. Today 51 (2021) 6–14, https://doi.org/10.1016/j.mattod.2021.10.025.

[46] S. Tanigawa, K. Hinode, R. Nagai, K. Kanbe, M. Doyama, N. Shiotani, Positron annihilation in amorphous alloys, Phys. Status Solidi A. 51 (1979) 249–255, https://doi.org/10.1002/pssa.2210510128.

[47] L.L. Snead, S.J. Zinkle, J.C. Hay, M.C. Osborne, Amorphization of SiC under ion and neutron irradiation, Nucl. Instrum. Methods Phys. Res. Sect. B Beam Interact. Mater. At. 141 (1998) 123–132, https://doi.org/10.1016/S0168-583X(98)00085-8.

[48] G. Amarendra, Positron annihilation studies of vacancy defects in crystalline and amorphous Si, Defect Diffus. Forum. 200–202 (2002) 189–218, https://doi.org/10.4028/www.scientific.net/DDF.200-202.189.

[49] M.-R. He, S. Wang, S. Shi, K. Jin, H. Bei, K. Yasuda, S. Matsumura, K. Higashida, I.M. Robertson, Mechanisms of radiation-induced segregation in CrFeCoNi-based single-phase concentrated solid solution alloys, Acta Mater. 126 (2017) 182–193, https://doi.org/10.1016/j.actamat.2016.12.046.

[50] S. Guo, C.T. Liu, Phase stability in high entropy alloys: Formation of solid-solution phase or amorphous phase, Prog. Nat. Sci. Mater. Int. 21 (2011) 433–446, https://doi.org/10.1016/S1002-0071(12)60080-X.

[51] R.J. Tilley, Understanding solids: the science of materials, John Wiley & Sons, 2004.

[52] A. Takeuchi, A. Inoue, Classification of bulk metallic glasses by atomic size difference, heat of mixing and period of constituent elements and its application to characterization of the main alloying element, Mater. Trans. 46 (2005) 2817–2829, https://doi.org/10.2320/matertrans.46.2817.

[53] C. Lu, L. Niu, N. Chen, K. Jin, T. Yang, P. Xiu, Y. Zhang, F. Gao, H. Bei, S. Shi, M.-R. He, I.M. Robertson, W.J. Weber, L. Wang, Enhancing radiation tolerance by controlling defect mobility and migration pathways in multicomponent single-phase alloys, Nat. Commun. 7 (2016) 13564, https://doi.org/10.1038/ncomms13564.

[54] Y.L. Zhao, T. Yang, Y. Tong, J. Wang, J.H. Luan, Z.B. Jiao, D. Chen, Y. Yang, A. Hu, C.T. Liu, J.-J. Kai, Heterogeneous precipitation behavior and stacking-fault-mediated deformation in a CoCrNi-based medium-entropy alloy, Acta Mater. 138 (2017) 72–82, https://doi.org/10.1016/j.actamat.2017.07.029.

[55] B.X. Liu, W.S. Lai, Z.J. Zhang, Solid-state crystal-to-amorphous transition in metal-metal multilayers and its thermodynamic and atomistic modelling, Adv. Phys. 50 (2001) 367–429, https://doi.org/10.1080/00018730110096112.

[56] S.J. Zinkle, Fusion materials science: Overview of challenges and recent progress, Phys. Plasmas. 12 (5) (2005) 058101, https://doi.org/10.1063/1.1880013.

[57] D.B. Miracle, O.N. Senkov, A critical review of high entropy alloys and related concepts, Acta Mater. 122 (2017) 448–511, https://doi.org/10.1016/j.actamat.2016.08.081.

[58] B.M. Clemens, Solid-state reaction and structure in compositionally modulated zirconium-nickel and titanium-nickel films, Phys. Rev. B. 33 (1986) 7615–7624, https://doi.org/10.1103/PhysRevB.33.7615.

[59] W. Jiang, Y. Zhang, W.J. Weber, Temperature dependence of disorder accumulation and amorphization in Au-ion-irradiated 6H−SiC, Phys. Rev. B. 70 (2004), https://doi.org/10.1103/PhysRevB.70.165208 165208.

[60] G.W. Yang, W.S. Lai, C. Lin, B.X. Liu, Irradiation-induced growth of nanoquasicrystals from amorphous matrix in the equilibrium immiscible Fe–Cu system, Appl. Phys. Lett. 74 (1999) 3305–3307, https://doi.org/10.1063/1.123326.

[61] B.X. Liu, Z.J. Zhang, O. Jin, A comparative study of metastable alloy formation by ion mixing and thermal annealing of multilayers in the immiscible Y-Zr system, J. Alloys Compd. 270 (1998) 186–193, https://doi.org/10.1016/S0925-8388(98)00494-0.

[62] X. Chen, Q. Wang, Z. Cheng, M. Zhu, H. Zhou, P. Jiang, L. Zhou, Q. Xue, F. Yuan, J. Zhu, X. Wu, E. Ma, Direct observation of chemical short-range order in a medium-entropy alloy, Nature 592 (2021) 712–716, https://doi.org/10.1038/s41586-021-03428-z.

[63] F.X. Zhang, S. Zhao, K. Jin, H. Xue, G. Velisa, H. Bei, R. Huang, J.Y.P. Ko, D.C. Pagan, J.C. Neuefeind, W.J. Weber, Y. Zhang, Local structure and short-range order in a NiCoCr solid solution alloy, Phys. Rev. Lett. 118 (2017), https://doi.org/10.1103/PhysRevLett.118.205501 205501.

[64] Y. Tong, K. Jin, H. Bei, J.Y.P. Ko, D.C. Pagan, Y. Zhang, F.X. Zhang, Local lattice distortion in NiCoCr, FeCoNiCr and FeCoNiCrMn concentrated alloys investigated by synchrotron X-ray diffraction, Mater. Des. 155 (2018) 1–7, https://doi.org/10.1016/j.matdes.2018.05.056.